Alma Mater Studiorum Università di Bologna
Archivio istituzionale della ricerca

Heterometallic rhodium clusters as electron reservoirs: Chemical, electrochemical, and theoretical studies of the centered-icosahedral [Rh12E(CO)27]n− atomically precise carbonyl compounds

(Article begins on next page)

Heterometallic rhodium clusters as possible nanocapacitors: chemical, electrochemical and theoretical studies of the centred-icosahedral [Rh$_{12}$E(CO)$_{27}$]$^{n-}$ atomically-precise carbonyl compounds.

Cristiana Cesari,[†] Cristina Femoni,*[†] Tiziana Funaioli,[ʃ] Maria Carmela Iapalucci,[†] Ivan Rivalta,[†γ] Silvia Ruggieri,*[†‡] Stefano Zacchini[†]

[†] Department of Industrial Chemistry "Toso Montanari", University of Bologna, Viale del Risorgimento, 4 – Bologna, Italy

[ʃ] Department of Chemistry and Industrial Chemistry, University of Pisa, Via Moruzzi 13, 56124 Pisa, Italy

[γ] Université de Lyon, École Normale Supérieure de Lyon, CNRS UMR 5182, Laboratoire de Chimie, 46 allée d'Italie, F69364 Lyon, France

[‡] Current address: Laboratory of Luminescent Materials, Department of Biotechnology, University of Verona, Strada Le Grazie, 15 – Verona, Italy

Abstract

In this paper we present a comparative study of the redox properties of the icosahedral [Rh$_{12}$E(CO)$_{27}$]$^{n-}$ (n = 4 when E = Ge or Sn; n = 3 when E = Sb or Bi) family of clusters through *in situ* infrared spectroelectrochemistry experiments and DFT computational studies. These clusters show shared characteristics in terms of molecular structure, being all E-centred icosahedral species, and electron counting, possessing 170 valence electrons as predicted by the electron-counting rules, based on the cluster-borane analogy, for compounds with such metal geometry. However, in some cases, clusters of similar nuclearity, and beyond, may show multivalence behaviour and be stable with a different electron counting, at least on the time scale of the electrochemical analyses. The experimental results, confirmed by theoretical calculations, showed a remarkable electron-sponge behaviour for [Rh$_{12}$Ge(CO)$_{27}$]$^{4-}$ (**1**), [Rh$_{12}$Sb(CO)$_{27}$]$^{3-}$ (**3**), [Rh$_{12}$Bi(CO)$_{27}$]$^{3-}$ (**4**), with a cluster charge going from −2 to −6 for **1** and **3**, and from −2 to −7 for cluster **4**, making them an example of molecular electron reservoirs. The [Rh$_{12}$Sn(CO)$_{27}$]$^{4-}$ (**2**) derivative, conversely, presents a limited ability to exist in separable reduced cluster species, at least within the experimental conditions, while in the gas phase it appears to be stable both as a pent- and hexa-anion, therefore showing a similar redox activity as its congeners. As a fallout of those studies, during the preparation of [Rh$_{12}$Sb(CO)$_{27}$]$^{3-}$ we were able to isolate a new species, namely [Rh$_{11}$Sb(CO)$_{26}$]$^{2-}$, which presents an incomplete Sb-centred icosahedral metal structure.

Introduction

Transition metal carbonyl clusters are a wide class of compounds with a variety of metal composition, nuclearity, geometry and chemical properties. Usually they adopt close-shell electronic configuration, so they exhibit an almost perfect correspondence between their number of Cluster Valence Electrons (CVEs) and metal structure. [1,2,3,4] These correspondences have been rationalized and modelled by exploiting the analogy with the borane chemistry, [5] and with the support of semiempirical calculations. [6] However, when certain *ad-hoc* conditions occur, they may exceptionally present multivalence behaviour, which means being able to reversibly accept and release electrons at given potential while maintaining their stability. [7] For instance, the presence of one or more interstitial metal atoms has proved to trigger such redox behaviour, as inner atoms strengthen the metal core by increasing the metal-metal interactions. The same role can be played by lighter carbon or nitrogen atoms in carbide and nitride species, respectively. [8] Moreover, doping of a metal cluster by inserting a different element may favourably alter the molecular orbital diagram so to facilitate electron addition/removal, not only in carbonyl clusters but also in gold nanoparticles. [9,10] A nuclearity of around ten-twelve metal atoms, and beyond, is also a common factor among carbonyl metal clusters with multivalence features, although some notable exceptions with lower nuclearity are known. [11,12] One of the most fascinating carbonyl species showing such properties is the $[Ni_{32}C_6(CO)_{32}]^{6-}$ hexanion, a pseudo-spherical carbide compound stabilized by carbonyl ligands showing a solely edge-bridging coordination, which can reversibly undergo one oxidation and four reduction monoelectronic steps. [13] Another notable example of redox activity involves the mixed-metal $[Os_{18}Pd_3C_2(CO)_{42}]^{2-}$ carbide cluster, [14] whose metal structure consists of two tri-capped carbide-centred octahedral joint by a triangular platinum unit. This species acts as an electron reservoir by accepting up to four extra electrons without significant decomposition. A similar electron-sponge behaviour has been reported for the Co-centred pentagonal antiprismatic $Co_{11}Te_7(CO)_{10}$ and $Co_{11}Te_5(CO)_{15}$ cluster anions. [15] More recently, heterometallic high nuclearity homoleptic Ni-Pd [16] and Rh-Sb, [17] and heteroleptic Au-Pd [18] and Au-Pt [19] nanoclusters – all possessing interstitial metal atoms – have proved to be multivalent. However, the high nuclearity and the interstitial atoms may not be *per se* sufficient to ensure such feature. For instance, the large heteroleptic $[Pd_{33}Ni_9(CO)_{41}(PPh_3)_6]^{4-}$ does not show multivalence, as the small cohesive energies of Pd-Pd and Pd-Ni bonding do not allow reversible redox changes to occur without metal-core breakdown. [20] Nonetheless, it is important to underline the fact that, despite some species seem to somehow escape the electron-counting rules based on the borane analogy, those rules still very well apply to metal carbonyl clusters for predicting the most stable electronic configuration in association with a given structural geometry.

In the last few years, [21] we were able to synthetize and characterize the icosahedral $[Rh_{12}E(CO)_{27}]^{n-}$ family of clusters, where E represents a post-transition metal (Sn, [22] Ge, [23] Sb, [24,25] and Bi [26]) and the negative charge varies from -4 to -3, depending on whether the metal belongs to group 14 or 15, respectively.

These clusters are not only isostructural but also isoelectronic, as they all possess 170 CVEs; moreover, they share the same synthesis, as they have been prepared by the same type of redox condensation reaction between a Rh-cluster precursor, namely $[Rh_7(CO)_{16}]^{3-}$,[27] and the heterometal halide. Considering their nuclearity, the presence of an interstitial metal atom, and in light of their many shared features, we decided to perform a comparative study on their ability to sustain addiction or depletion of electrons. Similar research by combining spectroelectrochemistry and cyclic voltametric experiments had been conducted in the past, for instance, to investigate the redox activity of the large $[Pt_{24}(CO)_{30}]^{n-}$, $[Pt_{26}(CO)_{32}]^{n-}$ and $[Pt_{38}(CO)_{44}]^{n-}$ (n = 0 to 10) homometallic carbonyl clusters.[28]

In the case of $[Rh_{12}E(CO)_{27}]^{n-}$ family of clusters, chemical experiments with reducing and oxidizing agents had been previously reported, but they had been inconclusive due to the lack of characterization of the obtained products. Conversely, spectroelectrochemical investigations reported here on the four clusters of this family showed a remarkable redox activity, and the results were confirmed by theoretical DFT calculations.

Finally, as a fallout of the performed studies, during the preparation of $[Rh_{12}Sb(CO)_{27}]^{3-}$ we were able to isolate a new species, namely $[Rh_{11}Sb(CO)_{26}]^{2-}$, which presents an incomplete Sb-centred icosahedral metal structure.

Results and Discussion

As mentioned before, in the past few years we exploited the redox condensation method for cluster synthesis to prepare several heterometallic rhodium carbonyl compounds.[21] A peculiarity that emerged after studying the Rh-Ge, Rh-Sn, Rh-Sb and Rh-Bi systems is that they have in common one specific isostructural species, obtained mostly through the same synthetic pathway, and also possessing the same number of CVEs. More specifically, the $[Rh_{12}E(CO)_{27}]^{n-}$ clusters (E = Ge, Sn, Sb, Bi; n = 3 or 4) consists of a centred-icosahedral metal frame made by the twelve Rh atoms, with the interstitial position always occupied by the heteroatom, and stabilized by the same number of carbonyl ligands. As for the anionic charge, this varies in accordance with the number of valence electrons carried by E; therefore, n is 4 when E belongs to group 14 (Ge and Sn), while it is equal to 3 if E belongs to group 15 (Sb and Bi). This way, all four $[Rh_{12}E(CO)_{27}]^{n-}$ clusters are not only isostructural but also isoelectronic, as they possess 170 CVEs, in compliance with the electron-counting rules. More in details, the valence electrons come from the twelve Rh atoms (12 x 9), the twenty-seven carbonyl groups (27 x 2), the interstitial atom (4 for Ge, Sn – or 5 for Sb, Bi) and the negative charge n (4 or 3, respectively).

Once we had the availability of such class of compounds, in consideration of their nuclearity and the presence of the interstitial metal atom, which represent key conditions that may indicate multivalence

properties, we decided to investigate the redox activity of all four clusters through electrochemistry, *in situ* infrared spectroelectrochemistry (IR SEC) experiments and DFT calculations.

The molecular structure of the $[Rh_{12}E(CO)_{27}]^{n-}$ cluster is illustrated in Figure 1.
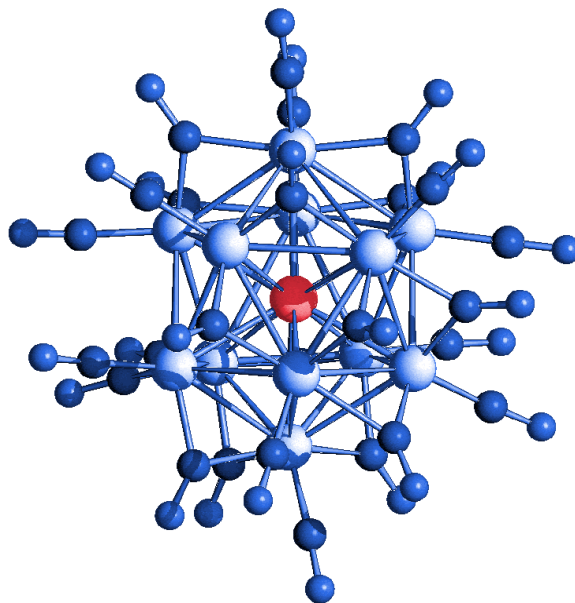

Figure 1. Molecular structure of the $[Rh_{12}E(CO)_{27}]^{n-}$ family of clusters (E is depicted in red).

The icosahedron described by the twelve Rh atoms shows some deviations from a regular polyhedron that are directly related to the interstitial-metal size. As a consequence, a less distorted geometry is observed for $[Rh_{12}Ge(CO)_{27}]^{4-}$ (**1**), being Ge the smallest heteroatom, whereas the farthest to the ideal polyhedron is that of $[Rh_{12}Bi(CO)_{27}]^{3-}$ (**4**), containing the largest Bi element. The remaining $[Rh_{12}Sn(CO)_{27}]^{4-}$ (**2**) and $[Rh_{12}Sb(CO)_{27}]^{3-}$ (**3**) are somewhere in between.In Table 1 the average distances for the Rh-Rh and Rh-E distances obtained from the crystallographic analyses are reported, along with the longest and shortest ones, as an indication of the extent of icosahedral distortion. We also inserted the Rh-Rh and Rh-E average distances obtained by DFT computations of isolated clusters in vacuum (all computed distances have been included in Table S1, in the SI section).

Bond lengths	$[Rh_{12}Ge(CO)_{27}]^{4-}$ (**1**)	$[Rh_{12}Sn(CO)_{27}]^{4-}$ (**2**)	$[Rh_{12}Sb(CO)_{27}]^{3-}$ (**3**)	$[Rh_{12}Bi(CO)_{27}]^{3-}$ (**4**)
Rh-Rh average (Å)	2.935 (3.088)	2.978 (3.120)	2.982 (3.129)	3.024 (3.169)
longest shortest	3.336 2.808	3.349 2.810	3.368 2.821	3.470 2.812
Rh-E average (Å)	2.788 (2.929)	2.830 (2.963)	2.823 (2.971)	2.859 (3.008)
longest shortest	2.929 2.645	2.933 2.741	2.941 2.707	2.978 2.736

Table 1. Average, longest and shortest Rh-Rh and Rh-E bond lengths observed in $[Rh_{12}E(CO)_{27}]^{n-}$. Both experimental and theoretical values are reported. The latter are in brackets.

The theoretical bond length values are consistently higher than the experimental ones of about 0.15 Å. This difference may be explained by the fact that the former values are associated with isolated $[Rh_{12}E(CO)_{27}]^{n-}$ clusters in gas phase, while the experimental data refer to a solid state where counterions, solvent molecules and packing effects are present.

Electrochemistry and IR spectroelectrochemistry

Electrochemical characterizations were performed on all four $[Rh_{12}E(CO)_{27}]^{n-}$ clusters in $CH_3CN/[N^nBu_4]PF_6$ solution, under either Ar or CO atmosphere, depending on the cluster stability. The cyclic voltammetric profiles registered at both Pt and Glassy Carbon (GC) showed low currents associated with the redox processes, which did not allow to obtain well-resolved peaks. These low currents did not depend on insufficient cluster solubility in the experimental conditions, as solutions with concentration higher than 1 mM could be prepared for all the compounds, and similar phenomena have been previously observed in other carbonyl clusters. [29] We are aware that the diagnostic criteria of the electrochemical and chemical reversibility of electron transfers, their formal potentials and the number of exchanged electrons can be straightforwardly obtained mainly by CV studies and controlled-potential coulometric measurements. However, from our experience, the presence of multiple stable redox states of a carbonyl cluster can be as clearly inferred by its *in situ* IR SEC studies, [30,31,32] conducted in an Optical Transparent Thin Layer Electrochemical (OTTLE) cell, [33] by the comparison between the sequence of IR spectra and the profile of the i/E curve. These curve profiles for $[Rh_{12}E(CO)_{27}]^{n-}$ family of clusters are reported in the Supporting Information section (Figure S1).

DFT computations on the four clusters are described in the following subsections to support the conclusions of the experimental studies.

The $[Rh_{12}Sb(CO)_{27}]^{3-}$ (3) cluster.

The *in situ* IR spectroelectrochemical measures for cluster **3** were performed under CO atmosphere to maintain the cluster stability. The IR spectra were recorded every 60 seconds. The first slow scan (1mV/sec) between +0.3 and −1.6 V (*vs* Ag pseudo-reference electrode), showed a shift of the CO stretching frequencies towards lower values upon reduction, as a result of the increased negative charge, and towards higher values under oxidation conditions (Figure 2).
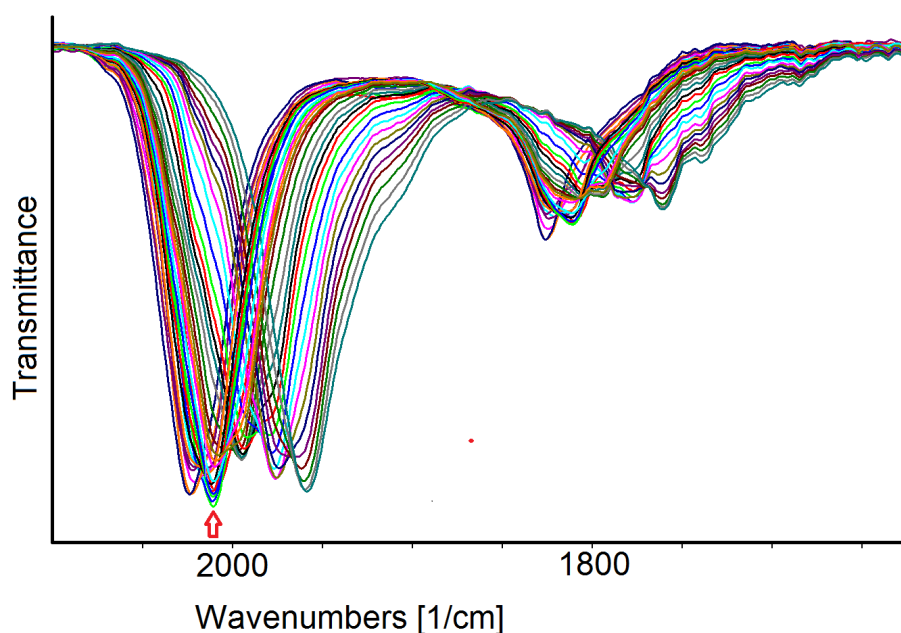
Figure 2. Infrared spectra of $[Rh_{12}Sb(CO)_{27}]^{3-}$ recorded in an OTTLE cell during the progressive decrease of the working electrode potential E from +0.3 to –1.6 V(*vs* Ag pseudo reference electrode) in CH_3CN containing 0.1 mol dm^{-3} $[N^nBu_4][PF_6]$. The solvent and supporting electrolyte absorptions have been subtracted. The red arrow indicates the initial spectrum.

These shifts were completely reversible, as demonstrated by the fact that an IR spectrum superimposable to the starting one was obtained in the reverse scan (Figure S2). A thorough analysis of the registered IR spectra and the i/E profile curve (Figure S1, yellow curve) made possible to separate the complete sequence in four groups, each belonging to a different redox step (Figure S3), and to identify five long-lived different negative charge states in which cluster **3** can exist: -2, -3, -4, -5 and -6. Their corresponding IR spectra are illustrated in Figure 3 and the related frequencies are reported in Table 2. The charge of each species was assigned considering mono-electronic steps, also considering that the shift values related to the stretching frequencies of terminal CO ligands are within a range of around 15-25 cm^{-1} per added/removed electron, which is a correspondence that has been previously ascertained for similar carbonyl clusters. [28] The presence of well-defined isosbestic points for each process, along with the quantitative restoration of the IR bands of the starting cluster, confirm the remarkable stability of **3** with different electron numbers.
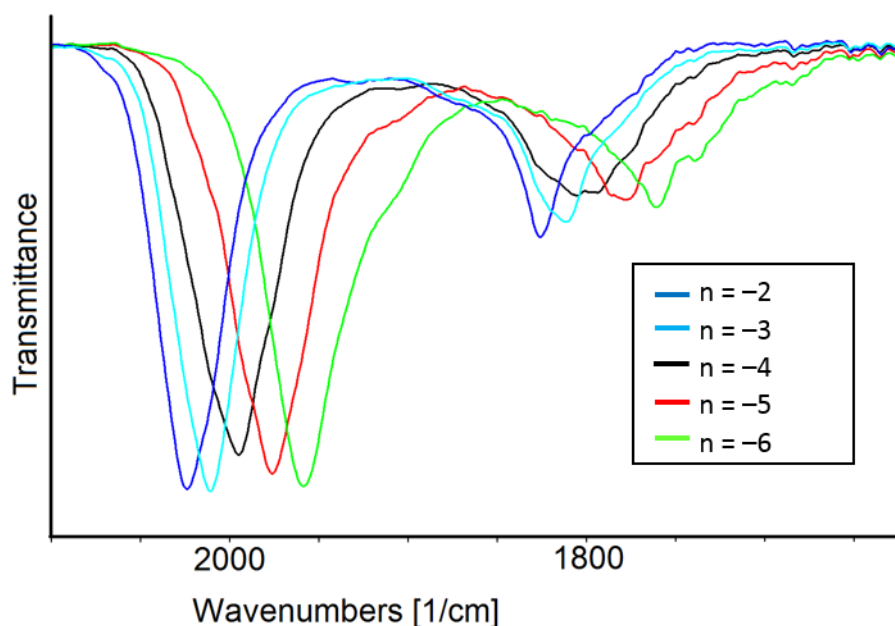
Figure 3. Selected infrared spectra of $[Rh_{12}Sb(CO)_{27}]^n$ as a function of the cluster charge n in CH_3CN containing 0.1 mol dm^{-3} $[N''Bu_4][PF_6]$. The absorptions of the solvent and supporting electrolyte have been subtracted.

Cluster charge n	ν^t_{CO} (cm^{-1})	ν^b_{CO} (cm^{-1})
−2	2025	1826
−3	2011	1812
−4	1995	1806
−5	1977	1778
−6	1959	1761

Table 2. Infrared stretching frequencies (cm^{-1}) of terminal (ν^t_{CO}) and bridging (ν^b_{CO}) carbonyl groups for **3** in CH_3CN solution as a function of the cluster charge.

When the potential was increased from +0.3 to +0.84 V, the oxidation of $[Rh_{12}Sb(CO)_{27}]^{2-}$ was followed by a relatively fast decomposition of the cluster, since the shift of the terminal CO band from 2025 to 2031 cm^{-1} (Figure S3e) was accompanied by a decrease of its intensity and the appearance of CO absorptions at 2120 and 2063 cm^{-1}, which are due to the formation of the mononuclear cationic $[Rh(CO)_2(CH_3CN)_2]^+$ complex. [34]

DFT computations were used to monitor the geometrical changes and the corresponding variations of IR spectra of the five long-lived charged states of cluster **3**, overall corroborating the interpretation of experimental evidence discussed above. Geometries optimizations of redox states with charges from −2 to −6 lead to stationary points representing stable local minima on the potential energy surfaces (PES), in agreement with their long-living nature. Notably, as shown in Figure 5 (see later) and Table S1, the Rh-Rh and the Rh-Sb bond distances increase systematically with the cluster charge, with −5 and −6

clusters featuring elongation of some Rh-Rh distances above 4.0 Å. A similar increase in the metal-metal bond distances with the increasing of the cluster charge had been previously observed for multivalent carbonyl compounds. [15]

While these highly charged clusters result thus partially distorted with respect to the $[Rh_{12}Sb(CO)_{27}]^{3-}$ crystal structure, their optimized geometries represent local minima on the PES, in agreement with their assignment as long-living species. In contrast, optimizing the structure with charge −7 led to cluster disassembling.

DFT simulated spectra of various charged states for cluster **3** (from −2 to −6) confirmed the systematic red/blue-shifts of the stretching frequencies of CO ligands (in a range of ca. 15-30 cm^{-1} per added/removed electron, respectively) observed experimentally, as shown in Figure S4 in the SI, corroborating the charge assignments based on mono-electronic redox steps for this cluster.

The $[Rh_{12}Bi(CO)_{27}]^{3-}$ (4) cluster.

The *in situ* IR SEC experiments for cluster **4** were carried out under Ar atmosphere, where the cluster is perfectly stable. The sequence of spectra showed in Figure 4 was collected in the potential range +0.4 ÷ −2.1 V (*vs* Ag pseudo-reference electrode) at scan rate of 2 mV sec^{-1}. No decomposition of the electrogenerated species was observed within that potential window and, moreover, the IR spectrum of the starting cluster was re-obtained when the working electrode potential returned to the initial value (Figure S5), indicating a full reversibility of the redox processes.

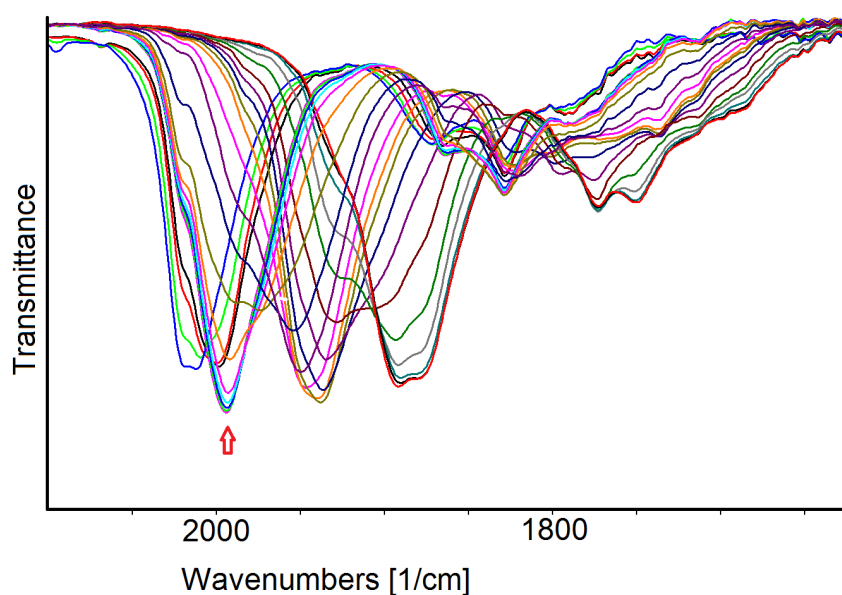**Figure 4**. Infrared spectra of $[Rh_{12}Bi(CO)_{27}]^{3-}$ recorded in an OTTLE cell during the progressive decrease of the working electrode potential E from +0.4 to −2.1 V(*vs* Ag pseudo reference electrode) in CH_3CN containing 0.1 mol dm^{-3} $[N^nBu_4][PF_6]$. The solvent and supporting electrolyte absorptions have been subtracted. The red arrow indicates the initial spectrum.

As suggested by the absorbance maxima of terminal and bridging CO bands and considering the stretching frequency of the initial tri-anion (indicated by the red arrow in Figure 4), the frequency shifts can be attributed to one oxidation and two reduction steps (Figure S6). However, only the oxidation is a mono-electronic process (Figure S6c), as the frequency downshifts with each reduction step are in the range of 40-50 cm^{-1}, around twice those observed for the cluster **3** system, suggesting that the observed reduction processes involve two electrons, leading to a −5 and then a −7 cluster charge. Moreover, the shift of the IR bands of **4** from 1994 to 1942 cm^{-1} registered between −0.4 and −1.3 V, corresponding to the first reduction process (the one from −3 to −5), occurred without a well-defined isosbestic point, and the complex pattern of the intermediate spectra suggested the presence of a transient additional negative state. The results of a spectral deconvolution performed on the middle spectrum of the reduction sequence (Figure S7) allowed us to determine the single absorbance contributions and unravelled the −4 cluster charge. The detailed description of this analysis is reported in the Supporting Information.

DFT computations indicate, indeed, that structural modifications of cluster **4** already start at charge −4 where a few Rh-Rh distances rise above 4.0 Å, as reported in Table S1 and depicted in Figure 5, and they continue more significantly at charge −6. Simulated IR spectra (Figure S4) however, indicate that such structural modifications are not significantly affecting the stretching of terminal and bridging CO groups, with overall spectral features quite similar to those computed for cluster **3**. Thus, DFT results would not fit with mono-electronic reductions associated to large (40-50 cm^{-1}) frequency red-shifts, corroborating the assignments of mono-electronic oxidation and bi-electronic reduction steps for the IR SEC experiments.
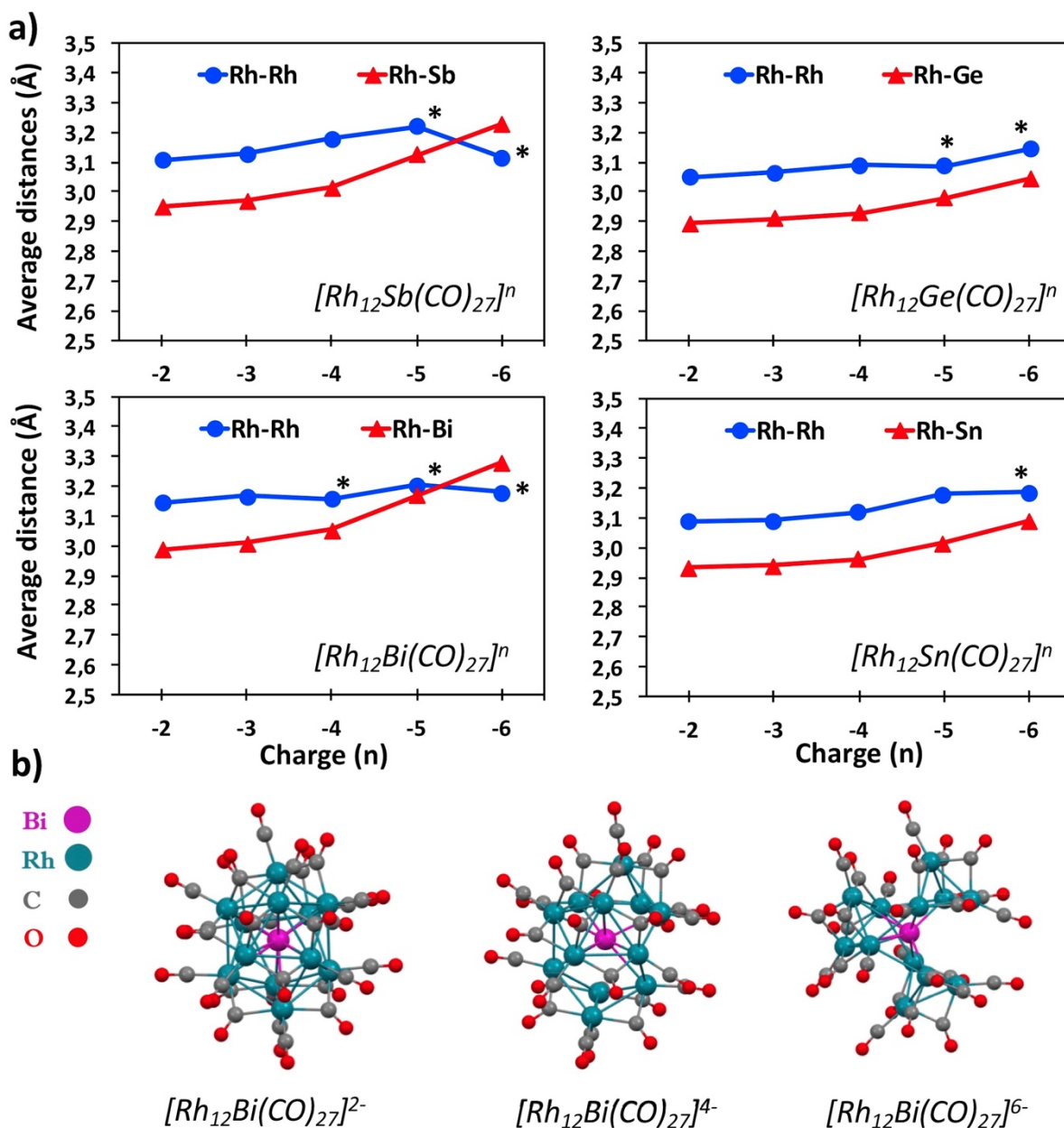
Figure 5. (a) Average Rh-Rh (in blue) and Rh-E (in red) bond distances (in Å) for clusters **1-4** at various redox states (charges from -2 to -6) computed using bond distances below 4 Å, using DFT optimized geometries. Distance averages indicated with asterisks (*) denote decrease of average values due to elongations of bond distances above 4 Å, thus excluded from the average computations. (b) DFT optimized geometries of clusters $[Rh_{12}Bi(CO)_{27}]^{n-}$, with $n = 2$, 4 and 6.

The selected experimental IR spectra for $[Rh_{12}Bi(CO)_{27}]^n$ ($n = -2, -3, -5, -7$) are shown in Figure 6, while Table 3 reports the CO stretching frequencies in solution associated with the cluster charge.

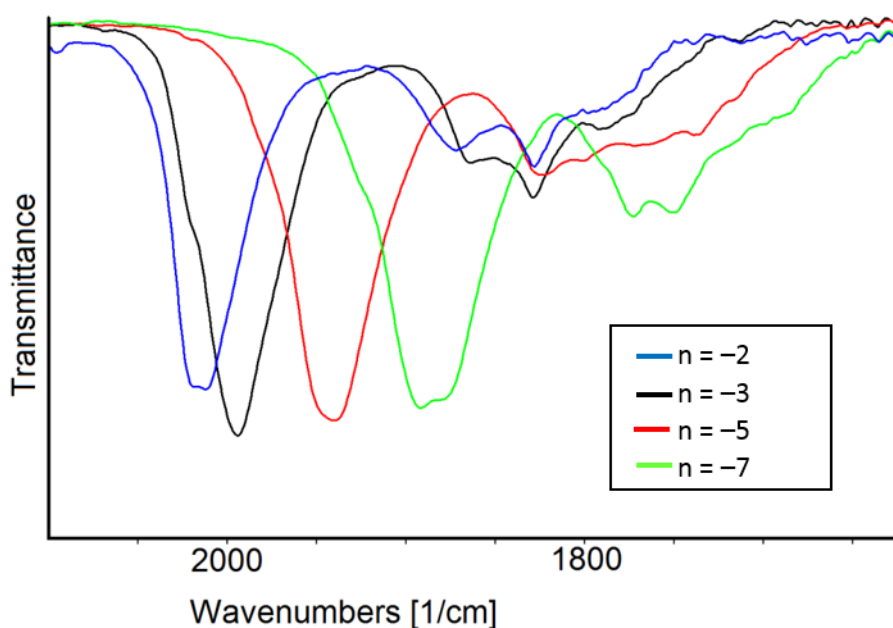**Figure 6**. Selected infrared spectra of $[Rh_{12}Bi(CO)_{27}]^n$ as a function of the cluster charge n in CH_3CN containing 0.1 mol dm^{-3} [N$''$Bu$_4$][PF$_6$]. The absorptions of the solvent and supporting electrolyte have been subtracted.

Cluster charge n	ν^t_{CO} (cm^{-1})	ν^b_{CO} (cm^{-1})
−2	2019, 2012	1872, 1828
−3	1994	1864, 1829, 1790
−4	*1967*	-
−5	1942	1823, 1801, 1772, 1736
−7	1892, 1879	1773, 1751

Table 3. Infrared stretching frequencies (cm^{-1}) of terminal (ν^t_{CO}) and bridging (ν^b_{CO}) carbonyl groups for **4** in CH_3CN solution as a function of the cluster charge. The row in italic corresponds to the cluster charge deduced by spectral deconvolution.

The [Rh$_{12}$Ge(CO)$_{27}$]$^{4-}$ (1) cluster

The *in situ* infrared spectroelectrochemical measures for cluster **1** were performed under CO atmosphere to ensure the cluster stability. The IR spectra were recorded every 60 seconds during a slow scan (1mV/sec), overall sweeping the potential between +0.8 and −1.8 V, as shown in Figure 7.

In the oxidation sequence up to +0.5 V (Figure 7a), in analogy with cluster **3** and **4,** the isosbestic points were well-defined and two reversible oxidation processes were observed. The differences in the stretching frequencies of the terminal CO ligands are in line with two mono-electronic oxidations. The spectral changes observed when increasing the potential up to +0.8 V indicated that a further oxidation is complicated by the decomposition of the cluster, leading to the [Rh(CO)$_2$(CH$_3$CN)$_2$]$^+$ complex (Figure 7b), like in the case of the Sb congener. When moving towards more negative potentials (Figure 7c), one reduction process occurred.
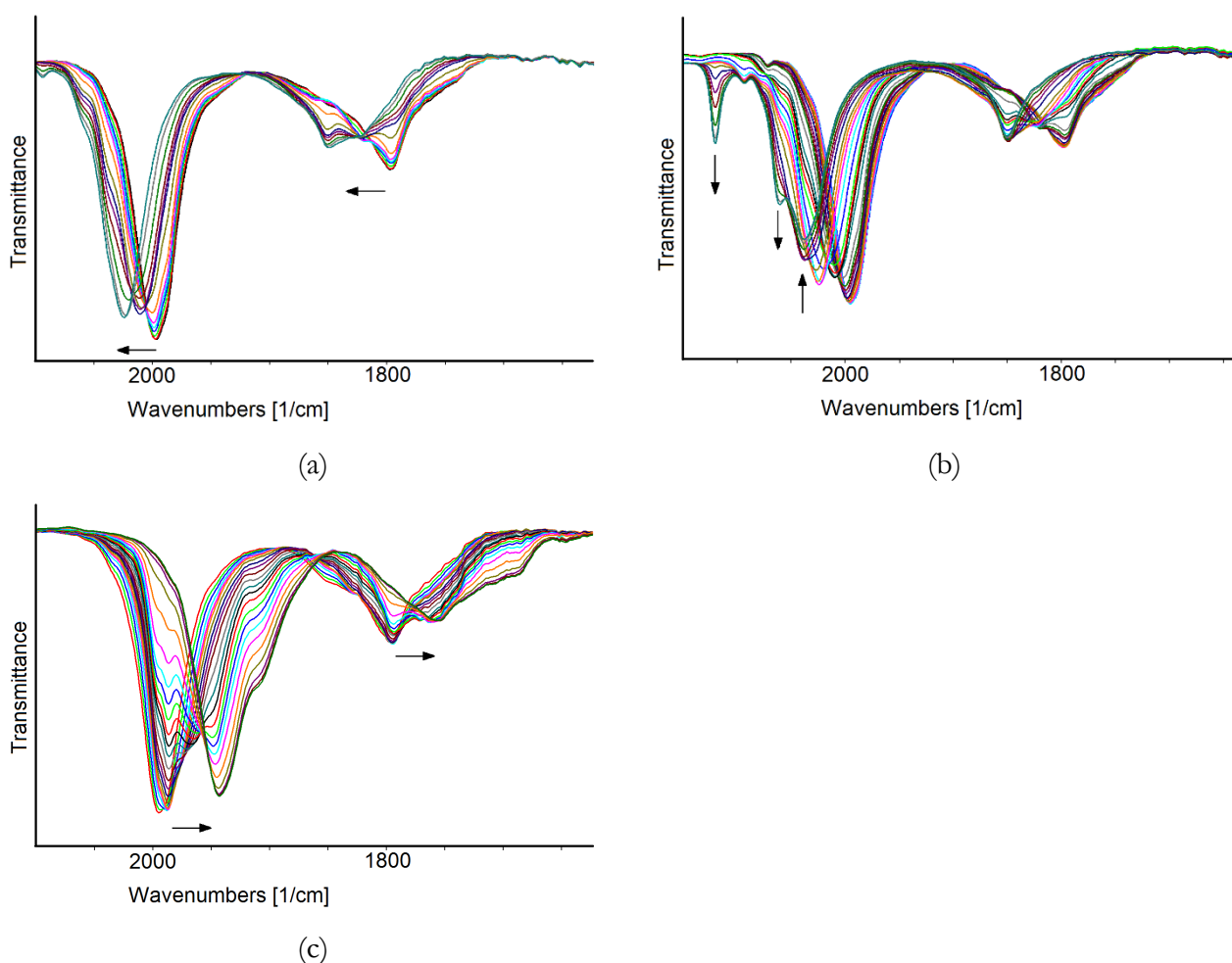
Figure 7. Infrared spectra of $[Rh_{12}Ge(CO)_{27}]^{4-}$ recorded in an OTTLE cell during the progressive increase working electrode potential E from (a) −0.3 to +0.5 V(*vs* Ag pseudo reference electrode), (b) −0.3 to +0.8 V(*vs* Ag pseudo reference electrode) and during the decrease of the working electrode potential E from (c) −0.4 to −1.8 V(*vs* Ag pseudo reference electrode), in CH_3CN containing 0.1 mol dm^{-3} $[N^nBu_4][PF_6]$. The solvent and supporting electrolyte absorptions have been subtracted.

It is important to note that when the potential scan was reversed, the chemical reversibility of the electron transfer was not complete and two new weak absorptions at 1905 and 1686 cm^{-1} appeared, (Figure S8) indicating a partial decomposition of the reduced cluster. The CO shifts in the reducing scan pointed to a two-electron process, leading to the $[Rh_{12}Ge(CO)_{27}]^{6-}$, thus indicating a preferred stability for even-electron species, in analogy with cluster **4**. However, the intermediate spectra in the reducing sequence show a complicated profile. A deconvolution analysis on a selected intermediate spectrum (Figure S9) could be matched by three main individual absorbance contributions, related to the −4, −5 and −6 cluster charges.

In conclusion, through the *in situ* IR spectroelectrochemical study of **1**, we were able to identify four long-lived different negative charge states (Figure 8) in which cluster **1** can exist: −2, −3, −4 (the initial one)

and −6, whose frequencies are reported in Table 4, and to gather evidences of the existence of one more species of limited stability with a −5 charge.
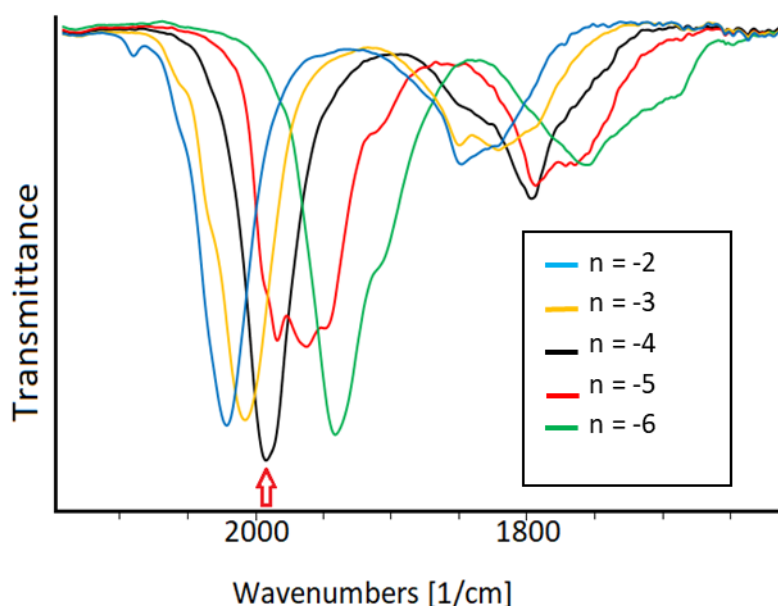

Figure 8. Selected infrared spectra of $[Rh_{12}Ge(CO)_{27}]^n$ as a function of the cluster charge n in CH_3CN containing 0.1 mol dm^{-3} $[N^nBu_4][PF_6]$. The absorptions of the solvent and supporting electrolyte have been subtracted.

Cluster charge n	v^t_{CO} (cm⁻¹)	v^b_{CO} (cm⁻¹)
n = −2	2024	1849
n = −3	2011	1851, 1822
n = −4	1996	1797
n = −5	*1966*	
n = −6	1943	1756

Table 4. Infrared stretching frequencies (cm⁻¹) of terminal (v^t_{CO}) and bridging (v^b_{CO}) carbonyl groups for **1** in CH_3CN solution as a function of the cluster charge. The row in italic corresponds to the cluster charge deduced by spectral deconvolution.

DFT calculations performed on cluster **1** confirmed that reductions to −5 and −6 charges are associated with partial deformations of the structure, in line with the partial decomposition observed experimentally for the reduced clusters. Overall, both Rh-Rh and Rh-E distances of **1** (E=Ge, group 14) are shorter than those of group 15 (**3** and **4**), as indicated in Table 1, and this trend is conserved along the corresponding redox series (Table S1 and Figure 5). DFT simulated IR spectra are in line with those of **3** and **4**, further confirming the presence of systematic shifts (< 30 cm⁻¹) of CO frequencies for mono-electronic redox steps, independently of E (Figure S4).

The [Rh₁₂Sn(CO)₂₇]⁴⁻ (2) cluster

The $[Rh_{12}Sn(CO)_{27}]^{4-}$ (2) cluster

The *in situ* IR spectroelectrochemical measures for cluster **2** were performed under Ar atmosphere, where the cluster is stable. The IR spectral changes recorded every 60 seconds during the potential sweep between +0.2 and −1.9 V (*vs* Ag pseudo-reference electrode) at the slow scan rate of 1 mV/sec are showed in Figure 9. The complete chemical reversibility of the observed electron changes was demonstrated since the spectrum of the starting cluster was regenerated in the reverse cycle of the potential, both after oxidation and reduction (Figure S10).
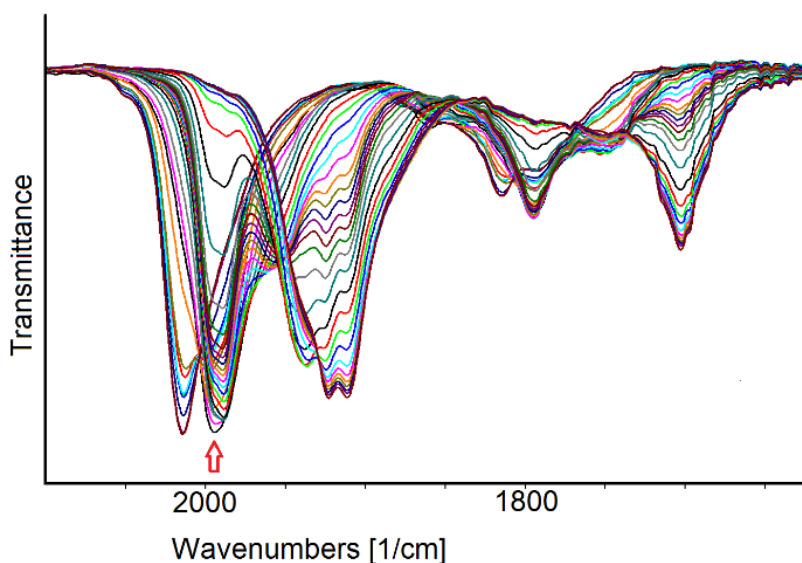

Figure 9. Infrared spectra of $[Rh_{12}Sn(CO)_{27}]^{4-}$ recorded in an OTTLE cell during the progressive decrease of the working electrode potential E from +0.2 to −1.9 V (*vs* Ag pseudo reference electrode) in CH_3CN containing 0.1 mol dm^{-3} [N*ⁿ*Bu₄][PF₆]. The absorptions of the solvent and supporting electrolyte have been subtracted. The red arrow indicates the initial spectrum.

In the oxidation sequence between −0.2 and +0.2 V, (Figure S11a), in analogy with what observed for the other Rh-Sb, Rh-Bi and Rh-Ge congeners, the isosbestic points are well-defined and one mono-electron oxidation process is recognizable. In the reduction sequence, up to −1.9 V (Figure S11b), on the contrary, there is not a net transformation of one charged species into the next reduced one.

Selected IR spectra of the whole sequence are shown in Figure 10. The black spectrum is related to the initial $[Rh_{12}Sn(CO)_{27}]^{4-}$ species, while the red one corresponds to the tri-anion; it is evident that upon oxidation the spectral shape has been perfectly retained. The green spectrum seems to indicate an intermediate passage between the starting tetra-anion and the subsequent reduction steps, in pale-blue and blue. Over the reduction processes, the spectral shape significantly changed, and the downshift magnitude of the first reduction step, calculated from the absorption maximum, indicates a two-electron process.
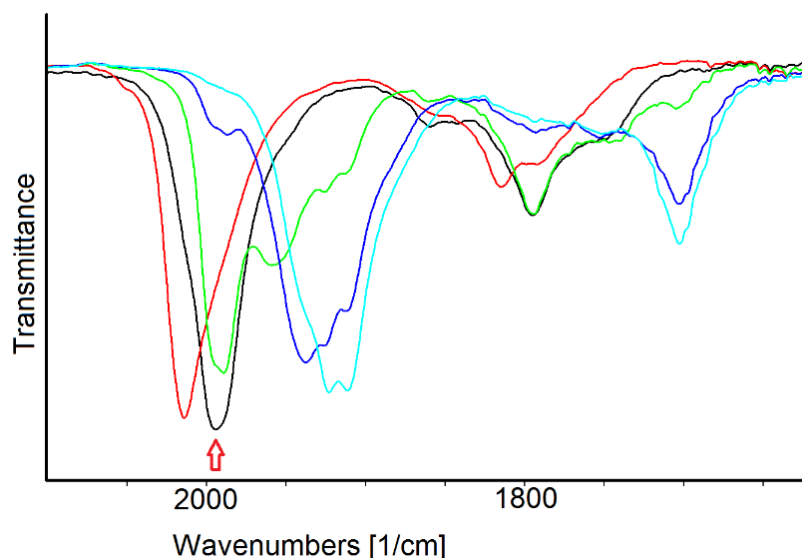
Figure 10. Selected IR spectra taken from the redox sequence reported observed over the potential sweep between +0.2 and −1.9 V

In conclusion, we can affirm that cluster **2** can undergo electron depletion and stably exist also as a tri-anion, as reported in Table 5. However, upon electron addition, the complicated IR pattern does not allow to properly identify as single species the more reduced states, at least on the timescale of the experimental conditions.

Cluster charge n	ν^t_{CO} (cm^{-1})	ν^b_{CO} (cm^{-1})
n = −3	2014	1815, 1793
n = −4	1995	1860, 1795, 1750

Table 5. Infrared stretching frequencies (cm^{-1}) of terminal (ν^t_{CO}) and bridging (ν^b_{CO}) carbonyl groups for **2** in CH$_3$CN solution as a function of the cluster charge.

The distance of the obtained IR spectra from the starting one towards more negative potentials may suggest that cluster **2** sustains significant, nonetheless reversible, structural modifications upon reduction. However, as the DFT simulated IR spectra (Figure S4) indicate that intramolecular structural deformations are not associated spectral shape alterations, the experimentally suggested structural changes could be related to interactions with solvent molecules, which are not explicitly considered in the DFT molecular models.

In fact, DFT geometry optimization and IR spectra of cluster **2** do not feature sizeable differences with respect to **1,** with elongation of Rh-Rh distances (around 4.0 Å and above) starting at charge −5 and present also at −6 (see Table S1 and Figure 5).

Synthesis and characterization of the $[Rh_{11}Sb(CO)_{26}]^{2-}$ (5) cluster.

During the synthesis of cluster **3**, which was carried out according to the literature, a new species that had not been previously detected was isolated in the tetrahydrofuran (THF) fraction. More specifically, at the end of the reaction the mother solution was dried under vacuum and the residue washed with water and then ethanol. In the present case, the latter extraction eliminated all the $[Rh(CO)_2Cl_2]^-$ complex obtained during the synthesis, unlike in the original procedure where the remaining of the complex was extracted in THF, being the following one in acetone that containing cluster **3**. Therefore, by analysing the IR spectrum in THF, peaks that were not attributable to any known species could be identified. It is likely that they had not been detected before as they might have been mixed with those of the Rh(I) complex, which are quite intense. Single crystals of the new species were obtained by layering hexane onto the THF solution, and the X-ray diffraction analysis allowed us to identify the new $[Rh_{11}Sb(CO)_{26}][NEt_4]_2\cdot THF$ (**5**$[NEt_4]_2\cdot THF$) carbonyl cluster.

Cluster **5** crystallizes in the monoclinic $P2_1/c$ space group. The unit cell contains four cluster units, eight tetraethylammonium cations and four THF solvent molecules. Its structure, illustrated in Figure 10 consists of an uncomplete Sb-centred icosahedron composed of the eleven Rh atoms, and stabilized by twenty-six carbonyl ligands, one less than the parent icosahedral species.
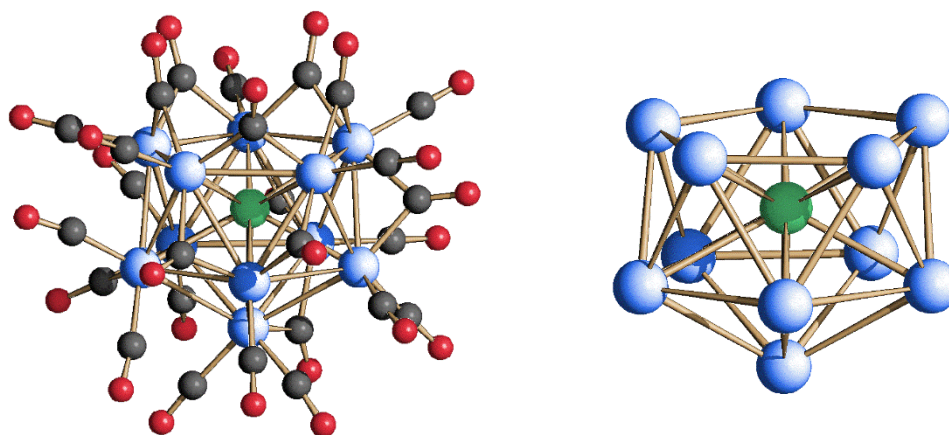
Figure 11. Molecular structure and metal skeleton of cluster **5**. Rh atoms are depicted in blue, Sb in green, C in grey and O in red.

The Rh-Rh distances vary from 2.8404(4) to 3.1133(4) Å (average 2.9427 Å), while the Rh-Sb bond lengths span from 2.6422(4) to 2.8654(4), with a mean value of 2.7933 Å. They are slightly shorter than those found in cluster **3**, most likely because of the minor metal skeleton distortion required for an open framework. Crystallographic data and most relevant bond lengths for cluster **5** are reported in the Supporting Information section (Table S2 and S3, respectively).

Cluster **5** was also characterized by electrospray ionization mass spectrometry (ESI-MS), by dissolving some crystals in acetonitrile. In the experimental conditions the molecular ion remained intact, with the exception of some CO losses that always occur in all Rh homo- and heterometallic clusters.

As for the electron counting, the $[Rh_{11}Sb(CO)_{26}]^{2-}$ cluster presents 158 CVEs given by the eleven rhodium atoms (11 x 9), the carbonyl ligands (26 x 2), the interstitial Sb atom (5), and the negative charge (2). The CVEs number is in perfect agreement with the electron-counting rules applied to a one-atom deficient (−12 CVEs) icosahedral cluster (170 CVEs).

Experimental Section

All reactions and compounds were handled using the standard Schlenk technique and under either nitrogen or carbon monoxide atmosphere. Solvents were dried and degassed before use, THF was dehydrated with Na-benzophenone and distilled under nitrogen. Halide salts of Ge, Sn, Sb and Bi were commercial products. The $[Rh_7(CO)_{16}]^{3-}$ cluster precursor, as well as the four $[Rh_{12}E(CO)_{27}]^{n-}$ compounds, were prepared according to literature. IR spectra were recorded on a PerkinElmer Spectrum One interferometer in CaF_2 cells.

Positive/negative-ion mass spectra were recorded in CH_3CN solutions on a Waters Micromass ZQ 4000 by using electrospray (ES) ionization. Experimental conditions: 2.56 kV ES-probe voltage, 10 V cone potential, 250 L h^{-1} flow of N_2 spray-gas, incoming-solution flow 20 μL min^{-1}.

Materials and apparatus for electrochemistry and IR SEC have been described elsewhere. [16] IR SEC measurements were performed on Ar-saturated $CH_3CN/[N^nBu_4]PF_6$ 0.1 M solutions of **2** (1.8 mM) or **4** (1.7 mM), and on CO-saturated $CH_3CN/[N^nBu_4]PF_6$ solutions of **3** (1.55 mM) or **1** (1.7 mM).

Computational details

All density functional theory (DFT) calculations were performed with the Gaussian 16 package [35] and employing the B3LYP exchange-correlation functional. [36,37,38] and using LANL2DZ basis set with pseudopotential for transition metals, [39] whereas 6-31G(d,p) basis set was used for the remaining atoms. [40] Geometry optimizations in vacuum were performed in combination with vibrational analysis in order to confirm the character of the stationary points and to simulate IR spectra, with vibrational frequencies computed analytically and rescaled using a 0.961 scaling factor. [41]

X-ray diffraction analysis

Single-crystal X-ray diffraction experiments were performed at 100 K on a Bruker Apex II diffractometer, equipped with a CCD detector, by using Kα-Mo radiation. Data were corrected for Lorentz polarization and absorption effects (empirical absorption correction SADABS). [42] Structures were solved by direct methods and refined by full-matrix least-squares based on all data using F^2. [43] Hydrogen atoms were fixed at calculated positions and refined by a riding model. All non-hydrogen atoms were refined with

anisotropic displacement parameters, including disordered atoms. Structure drawings were made with SCHAKAL99. [44] In order to obtain a better structural model, the cations and the THF molecule were treated as positionally disordered and each was split in two positions, using the necessary anisotropic displacement parameter restraints.

Synthesis of $[Rh_{11}Sb(CO)_{26}]^{2-}$ (5)

An acetonitrile solution of $SbCl_3$ (0.104 g, 0.46 mmol) was slowly added to a solution of $[Rh_7(CO)_{16}][NEt_4]_3$ (0.950 g, 0.61 mmol) in the same solvent, under CO atmosphere, and in a 0.75:1 molar ratio, respectively. After 3 hours the resulting brown solution was dried under vacuum and the solid washed with water (120 mL) and ethanol (100 mL). $[Rh_{11}Sb(CO)_{26}]^{2-}$ was extracted in THF (10 mL) and by layering hexane on the solution, black crystals of $[Rh_{11}Sb(CO)_{26}][NEt_4]_2 \cdot THF$ (yield ≈ 15% based on Rh) were obtained. Cluster **5** is well-soluble in THF, acetone, acetonitrile and DMF, and it is stable in water. Its IR spectrum recorded in CH_3CN shows νCO absorptions at 2033(vs), 1869(mw), and 1813(mw) cm^{-1}. ESI-MS analysis performed in an acetonitrile solution of **5** shows characteristic signal at 963 m/z, assigned to the $[Rh_{11}Sb(CO)_{24}]^{2-}$ ion, plus other consecutive signals due to CO loss (Figure S11).

Conclusions

In this paper we presented a comparative study via spectroelectrochemical experiments and theoretical calculations of the redox properties of the icosahedral $[Rh_{12}E(CO)_{27}]^{n-}$ (n = 4 when E = Ge or Sn; n = 3 when E = Sb or Bi) family of clusters, which have shared characteristics in terms of molecular structure, being all E-centred icosahedral species, and electron counting, possessing 170 CVEs. The results showed a remarkable multivalence behaviour for all clusters, albeit with some important differences, making them an example of molecular electron reservoirs.

The most redox active species is $[Rh_{12}Sb(CO)_{27}]^{3-}$ (**3**), which can stably exist with five different negative charges, from −2 to −6 (going from 169 to 173 CVEs), both from the experimental and theoretical point of view. The $[Rh_{12}Bi(CO)_{27}]^{3-}$ (**4**) compound presents an experimental behaviour previously observed in other carbonyl clusters, more specifically it seems to be more stable with an even number of CVEs, at least in the reduced form. Therefore, while the di-anion (169 CVEs) can be fully generated and isolated within the electrochemical experiments, the reduction from the initial tri-anion seems to favour the formation of the penta- (172 CVEs) and then epta-anionic (174 CVEs) congeners, resulting in a total of four different negative charges in which cluster **4** can stably exist. The intermediate fifth species with 171 CVEs ($[Rh_{12}Bi(CO)_{27}]^{4-}$) could not be isolated within the electrochemical experiments, even if its IR spectrum can be obtained by spectral deconvolution, but its existence was predicted by DFT

computational studies. As for the $[Rh_{12}Ge(CO)_{27}]^{4-}$ (**1**) cluster, again the depletion of electrons leads to the stable tri- and di-anions (with 169 and 168 CVEs, respectively), while under reduction it is possible to isolate it only with an even number of electrons up to the hexa-anion (172 CVEs), giving a total of four different cluster charges. The existence of the fifth odd-electron $[Rh_{12}Ge(CO)_{27}]^{5-}$ species, however, was confirmed by theoretical calculations, and its IR spectrum could be obtained by spectral deconvolution analysis.

The more complicated behaviour is that of $[Rh_{12}Sn(CO)_{27}]^{4-}$ (**2**), as it only clearly shows one stable oxidation process in solution leading to the tri-anion (169 CVEs), while its more reduced congeners cannot be properly isolated one from the other, even if the theoretical calculations predict the cluster stability in the gas phase up to the hexa-anion.

One important outcome emerging from this study is the importance of the performed theoretical calculations in corroborating the hypothesis deducible from the experimental results. In fact, for all species, the experimental stretching frequency shifts related to the carbonyl ligands assigned to mono-electronic processes are within the 15-25 cm^{-1} range, and the theoretical ones always of around 20-30 cm^{-1} for the same redox processes. This correspondence validates the assignments of mono-electronic steps within the experimental conditions, even in the absence of well resolved peaks in the CV profiles due to low currents, like in the present case.

Another significant result is that, by analysing the DFT simulated spectra of all clusters with different charges, even in presence of significant intramolecular structural modifications of DFT optimized structures, the IR spectral shape is always maintained (see Figure S4). This suggests that, wherever there was a reversible spectral modification in solution, this could be due to either interactions with the solvent, or the co-existence of more than one species.

Finally, from the analysis of the molecular structure of **5**, it could be speculated that this cluster represents an intermediate species within the growing path of cluster **3**, at least from a structural point of view. However, this cannot be ascertained as the growing mechanism of high-nuclearity metal carbonyl clusters is still a challenge, as it is driven by different contributions involving, among others, metal-metal and metal-ligand bond energies and electronic stability. [45,46]

Supporting Information

Rh-Rh and Rh-E bond distances for clusters 1-4 at various redox in DFT optimized (Table S1)

CV profiles of the four $[Rh_{12}E(CO)_{27}]^{n-}$ clusters (Figure S1).

IR spectra of $[Rh_{12}Sb(CO)_{27}]^{3-}$ before and after CV experiments (Figure S2); IR spectral sequences of $[Rh_{12}Sb(CO)_{27}]^{n-}$ during the progressive decrease and increase of potential E (Figure S3).

DFT simulated IR spectra for clusters 1-4 at various redox states (Figure S4).

IR spectra of $[Rh_{12}Bi(CO)_{27}]^{3-}$ before and after CV experiments (Figure S5); IR spectral sequences of $[Rh_{12}Bi(CO)_{27}]^{n-}$ during the progressive decrease and increase of potential E (Figure S6); Spectral deconvolution of the intermediate sequence in the first reduction sequence of $[Rh_{12}Bi(CO)_{27}]^{3-}$ (Figure S7).

IR spectra of $[Rh_{12}Ge(CO)_{27}]^{4-}$ before and after CV experiments (Figure S8); Spectral deconvolution of the red IR spectrum in Figure 8 for $[Rh_{12}Ge(CO)_{27}]^{n-}$ (Figure S9)

IR spectra of $[Rh_{12}Sn(CO)_{27}]^{4-}$ before and after CV experiments (Figure S10); IR spectral sequences of $[Rh_{12}Sn(CO)_{27}]^{n-}$ during the progressive decrease and increase of potential E (Figure S11).

ESI-MS spectrum of $[Rh_{11}Sb(CO)_{26}]^{2-}$ (Figure S12); Crystallographic data for $[Rh_{11}Sb(CO)_{26}]^{2-}$ (Table S2); Most relevant bond lengths for $[Rh_{11}Sb(CO)_{26}]^{2-}$ (Table S3).

Cartesian coordinates of DFT optimized geometries for clusters 1-4 at various redox states.

Accession Codes

CCDC 2088391 contain the supplementary crystallographic data for cluster 5. Data can be obtained free of charge via www.ccdc.cam.ac.uk/data_request/cif, or by emailing data_request@ccdc.cam.ac.uk, or by contacting The Cambridge Crystallographic Data Centre, 12 Union Road, Cambridge CB2 1EZ, UK; fax: +44 1223 336033.

Data Availability

The data that supports the findings of this study are available within the article [and its supplementary material].

References

1   D. F. Shriver, D. K Herbert, and R. D. Adams, The Chemistry of Metal Cluster Complexes, VCH: New York, USA, 1990.

2   G. Schmid (Ed.), Clusters and Colloids: From Theory to Applications, VCH, Weinheim, 1994.

3   L. J. De Jongh (Ed.), Physics and Chemistry of Metal Cluster Compounds, Kluwer, Dordrecht, 1994.

4   P. Braunstein, L.A. Oro, and P.R. Raithby (Eds.), Metal Clusters in Chemistry, Wiley–VCH, Weinheim, 1999.

5   D. M. P. Mingos, Acc. Chem. Res. 17, 311 (1984).

6   B. K. Teo, Inorg. Chem. 23, 1251 (1984).

7   C. Femoni, M. C. Iapalucci, F. Kaswalder, G. Longoni, and S. Zacchini, Coord. Chem. Rev. 250, 1580 (2006).

8   A. Fumagalli, P. Ulivieri, M. Costa, O. Crispu, R. Della Pergola, F. Fabrizi de Biani, F. Laschi, P. Zanello, P. Macchi, and A. Sironi, Inorg. Chem. 43, 2125 (2004).

9   K. Kwak, and Dongil Lee, Acc. Chem. Res. 52, 12 (2019).

10 R. Jin, C. Zeng, M. Zhou, and Y. Chen, Chem. Rev. 116, 10346 (2016).

11 G. Longoni, M. Manassero, and M. Sansoni, J. Am. Chem. Soc. 102, 7973 (1980).

12 R. D. Adams, I. Arafa, G. Chen, J-C Lii, and J-G. Wang, Organometallics 9, 2350 (1990).

13 F. Calderoni, F. Demartin, F. Fabrizi de Biani, C. Femoni, M. C. Iapalucci, G. Longoni, and P. Zanello, Eur. J. Inorg. Chem. 663 (1999).

14 K.-F. Yung, and W.-T. Wong, Angew. Chem. Int. Ed. 42, 553 (2003)

15 C. Olivier, H. Cattey, J.-F. Halet, W. Meier, Y. Mugnier, J. Wachter, J.-Y. Saillard, B. Zouchoune, and Manfred Zabel, Inorg. Chem. 46, 501 (2007).

16 B. Berti, C. Cesari, C. Femoni, T. Funaioli, M. C. Iapalucci, and S. Zacchini Dalton Trans. 49, 5513 (2020).

17 C. Femoni, T. Funaioli, M. C. Iapalucci, S. Ruggieri, and S. Zacchini, Inorg. Chem. 59, 4300 (2020).

18 N. T. Tran, D. R. Powell, and Lawrence F. Dahl, Dalton Trans. 4, 209 (2004).

19 A. Ceriotti, P. Macchi, A. Sironi, S. El Afefey, M. Daghetta, S. Fedi, F. Fabrizi de Biani, and R. Della Pergola, Inorg. Chem. 52, 1960 (2013).

20 M. Kawano, J. W. Bacon, C. F. Campana, B. E. Winger, J. D. Dudek, S. A. Sirchio, S. L. Scruggs, U. Geiser, and L. F. Dahl, Inorg. Chem. 40, 2554 (2001)

21 C. Femoni, M. C. Iapalucci, S. Ruggieri, and S. Zacchini, Acc. Chem. Res. 51, 2748 (2018).

22 C. Femoni, M. C. Iapalucci, G. Longoni, C. Tiozzo, S. Zacchini, B. T. Heaton, and J. A. Iggo, Dalton Trans. 35, 3914 (2007).

23 A. Boccalini, P. J. Dyson, C. Femoni, M. C. Iapalucci, S. Ruggieri, and S. Zacchini, Dalton Trans. 47, 15737 (2018).

24 J. L. Vidal, and J. M. Troup, J. Organomet. Chem. 213, 351 (1981).

25 C. Femoni, I. Ciabatti, M. C. Iapalucci, S. Ruggieri, and S. Zacchini, Pro. Nat. Sci-Mater. 26, 461 (2016).

26 C. Femoni, G. Bussoli, I. Ciabatti, M. Ermini, M. Hayatifar, M. C. Iapalucci, S. Ruggieri, and S. Zacchini, Inorg. Chem. 56, 6343 (2017)

27   S. Martinengo, and P. Chini, Gazz. Chim. It. 102, 344 (1972).

28   J. D. Roth, G. J. Lewis, L. K. Safford, X. Jiang, L. F. Dahl, M. J. Weaver, J. Am. Chem. Soc. 114, 6159 (1992).

29   B. Berti, C. Cesari, C. Femoni, T. Funaioli, M. Carmela Iapalucci, and Stefano Zacchini, Dalton Trans. 49, 5513 (2020)

30   R. Della Pergola, M. Bruschi, A. Sironi, M. Manassero, C. Manassero, D. Strumolo, S. Fedi, and P. Zanello Dalton Trans. 40, 5464 (2011).

31   A. Albinati, F. Balzano, F. Fabrizi de Biani, P. Leoni, G. Manca, L. Marchetti, S. Rizzato, G. Uccello Barretta, and P. Zanello, Inorg. Chem. 49, 3714 (2010).

32   O. F. Koentjoro, P. J. Low, R. Rousseau, C. Nervi, D. S. Yufit, J. A. K. Howard, and K. A. Udachin, Organometallics 24, 1284 (2005).

33   M. Krejčik, M. Daněk, and F. Hartl J. Electroanal. Chem. Interfacial Electrochem. 317, 179 (1991).

34   M. E. Prater, L.E. Pence, R. Clèrac, G.M. Finniss, C. Campana, P. Auban-Senzier, D. Jèrome, E. Canadell, and K. R. Dunbar, J.A.C.S. 121, 8005 (1999).

35   M. J. Frisch, et al., Gaussian Revision C.01, Gaussian, Inc., Wallingford CT, 2016.

36   A. D. Becke, J. Chem. Phys. 98, 5648 (1993).

37   C. Lee, W. Yang, and R. G. Parr, Rev. B: Condens. Matter Mater. Phys. 37, 785 (1988).

38   M. Dolg, U. Wedig, H. Stoll, and H. Preuss J. Chem. Phys. 86, 866 (1987)

39   Hay P. J. and W. R. Wadt, J. Chem. Phys. 82, 299 (1985).

40   M. M. Francl, W. J. Pietro, W. J. Hehre, J. S. Binkley, D. J. DeFrees, J. A. Pople, and M. S. Gordon, J. Chem. Phys. 77 3654 (1982).

41   NIST Computational Chemistry Comparison and Benchmark Database, NIST Standard Reference Database Number 101, Release 21, August 2020, Editor: Russell D. Johnson III, http://cccbdb.nist.gov

42   Sheldrick, G. M. SADABS, Program for empirical absorption correction, University of Göttingen, Germany, 1996.

43   Sheldrick, G. M. SHELX 2014/7, Program for crystal structure determination, University of Göttingen, Germany, 2014.

44   Keller, E. SCHAKAL99, University of Freiburg, Germany, 1999.

45   K. Wade, Inorg. Nucl. Chem. Letters 14, 71 (1978).

46   A. K Hughes, and K. Wade, Coord. Chem. Rev. 197, 191 (2000).

TOC